MATERIALS SCIENCE

Self-organization of nanoparticles and molecules in periodic Liesegang-type structures

Amanda J. Ackroyd[1], Gábor Holló[2], Haridas Mundoor[3], Honghu Zhang[4], Oleg Gang[4,5], Ivan I. Smalyukh[3], István Lagzi[4,6]*, Eugenia Kumacheva[1,7,8]*

Chemical organization in reaction-diffusion systems offers a strategy for the generation of materials with ordered morphologies and structural hierarchy. Periodic structures are formed by either molecules or nanoparticles. On the premise of new directing factors and materials, an emerging frontier is the design of systems in which the precipitation partners are nanoparticles and molecules. We show that solvent evaporation from a suspension of cellulose nanocrystals (CNCs) and L-(+)-tartaric acid [L-(+)-TA] causes phase separation and precipitation, which, being coupled with a reaction/diffusion, results in rhythmic alternation of CNC-rich and L-(+)-TA–rich rings. The CNC-rich regions have a cholesteric structure, while the L-(+)-TA–rich bands are formed by radially aligned elongated bundles. The moving edge of the pattern propagates with a finite constant velocity, which enables control of periodicity by varying film preparation conditions. This work expands knowledge about self-organizing reaction-diffusion systems and offers a strategy for the design of self-organizing materials.

INTRODUCTION

Self-organization and self-assembly in non-equilibrium systems are a universal process that occurs in living matter (*1*, *2*), geochemical and mineralogical environments (*3*), materials science (*4*), and industrial settings (*5*). In particular, patterns formed in reaction-diffusion systems provide a fascinating example of highly ordered, spatial or spatiotemporal structures as a result of the synergy between transport of chemical species and chemical reactions. For example, periodic ring patterns have been observed in seemingly unrelated systems, e.g., in crystallizing low–molecular weight compounds (*6*), polymer films formed from solutions (*7*, *8*), emulsion polymerization mixtures (*9*), and even in human tissues (*10*). In crystallizing polymer melts, the formation of ring-banded spherulites due to the helicoidal twisting of radial lamellae is a commonly observed phenomenon (*11*).

A special class of reaction-diffusion systems is that in which a heterogeneous precipitation pattern forms. In a reaction-diffusion experiment conducted by Liesegang in the late 19th century, a reaction between two water-soluble electrolytes resulted in spatially periodic ring-type bands of a precipitating salt (*12*). Periodic precipitation originated from coupling of the rates of the precipitation process and reactant mass transport, resulting in a reactant-exhausted medium (*13*).

Currently, experiments leading to periodic structures can be divided into two groups. In the classical Liesegang-type experiments, the system consists of two interacting components [ions or oppositely charged nanoparticles (NPs)], which are initially spatially separated (*4*, *14*). Pattern formation occurs due to diffusion of these components toward each other, leading to the first precipitation band when the product of local concentrations of the reagents exceeds the solubility product. The precipitation process decreases the reagent concentrations in the precipitation zone faster than the diffusion can increase them, causing depletion, thus depleting the reagents in the region surrounding the first precipitation band. A new precipitation band forms once the solubility product is exceeded again. The repetition of the precipitation process yields periodic precipitate bands. In the second group of experiments, periodic ring-type structures form in a system that initially has a spatially uniform distribution of components but undergoes phase separation or crystallization (*15*, *16*).

Chemical organization via periodic precipitation offers a new strategy for the generation of materials with ordered morphologies and structural hierarchy (*17*, *18*). Molecular self-organization on nano- to micrometer length scales via the reaction-diffusion process has already led to proof-of-concept applications of periodically structured materials in optics (*19*), microfluidics (*20*), and drug release systems (*21*). An emerging frontier in this field is the design of reaction-diffusion systems in which the precipitation partners are nanocolloidal building blocks or a combination of NPs and molecules (*4*) rather than reacting molecules. The capability to organize NP building blocks into well-defined, ordered patterns offers the capability to create hierarchically organized nanostructures with functionality stemming from the synergistic properties of NP assemblies (*22*). The first step in this direction has been undertaken by coprecipitating oppositely charged metal NPs that played the role of two "electrolytes" in a Liesegang-type system (earlier described as group 1) (*23*). Upon neutralization of the NP charges, colloidal stability of the system was lost, and NPs precipitated into periodic concentric zones. The next step in the organization of NPs includes periodic precipitation on the premise of new directing factors (*24*) and film compositions over different length scales, thereby offering a higher complexity in self-organization and following nature-made periodic patterns (*25*).

Here, we report periodic precipitation patterns formed by the colloidal and molecular components, namely, cellulose nanocrystals (CNCs) and L-(+)-tartaric acid [L-(+)-TA]. CNCs, rod-shaped NPs

[1]Department of Chemistry, University of Toronto, Toronto, ON M5S 3H6, Canada. [2]BME-MTA Condensed Matter Physics Research Group, Budapest H-1111, Hungary. [3]Department of Physics, Materials Science and Engineering and Renewable and Sustainable Energy Institute (RASEI), University of Colorado, Boulder, CO 80309, USA. [4]Center for Functional Nanomaterials, Brookhaven National Laboratory, Upton, NY 11973, USA. [5]Departments of Chemical Engineering and Applied Physics and Applied Mathematics, Columbia University, New York, NY 10027, USA. [6]Department of Physics, Budapest University of Technology and Economics, Budapest H-1111, Hungary. [7]Department of Chemistry, Institute of Biomaterials and Biomedical Engineering, University of Toronto, Toronto, ON M5S 3H6, Canada. [8]Department of Chemical Engineering and Applied Chemistry, University of Toronto, Toronto, ON M5S 3H6, Canada.
*Corresponding author. Email: eugenia.kumacheva@utoronto.ca (E.K.); istvanlagzi@gmail.com (I.L.)

with a length of 100 to 300 nm and diameter of 10 to 20 nm (*26*), have recently attracted great interest of the soft matter and materials science community because of their ability to organize into cholesteric (Ch) liquid crystals (*27*). Upon drying, aqueous CNC suspensions mixed with low–molecular weight molecules (*28*, *29*), polymers (*30*, *31*) and NPs (*32*–*34*) formed films with either a Ch structure (with intrinsic defects) or random disordered morphologies; however, periodic precipitation bands have not been reported.

In the present work, we show that upon solvent evaporation, an aqueous L-(+)-TA/CNC mixture undergoes phase separation and subsequent precipitation, which, being coupled with a diffusion-driven process, results in a rhythmic alternation of CNC-rich and CNC-depleted [or L-(+)-TA–rich] ring-type regions. The CNC-rich regions had a Ch structure with characteristic optical properties, while the L-(+)-TA–rich regions exhibited anisotropy stemming from radially aligned bundles. The propagation of the front edge of the ring-banded pattern with a constant velocity yielded periodic structures, with a period controlled by film composition and water evaporation rate, that is, ambient relative humidity (RH). The developed kinetic model was in qualitative agreement with the experimental results. Our results expand the range of self-organizing reaction-diffusion systems and pave the way for the design of periodically structured functional materials.

RESULTS

We used CNCs with an average length and diameter of 176 and 21 nm, respectively, degree of sulfation of 330.1 ± 0.5 mmol/kg, and electrokinetic potential (ζ-potential) of −44.1 ± 2.2 mV (see Materials and Methods). Composite films were formed from aqueous L-(+)-TA/CNC suspensions at RH in the range from 18 to 39% at 22°C at the ratio of mass concentrations of TA to CNCs, R, in the range of $0 \leq R \leq 9.0$. Upon addition of L-(+)-TA to the CNC suspension, the ζ-potential of CNCs reduced, e.g., at $R = 5.0$, it was −23.4 ± 0.7 mV.

Mixed suspensions were deposited as 10-μl droplets on glass slides, which were immediately placed in a humidity chamber. Figure 1 (A to E) shows polarizing optical microscopy (POM) images of the films formed by drying L-(+)-TA/CNC suspensions with varying compositions, as well as the films formed from the CNC suspension and L-(+)-TA solution, used as control systems. Images of birefringent CNC films (Fig. 1A) exhibited a characteristic Maltese cross, which indicated that the CNCs arranged in a symmetric, radial pattern (*35*). Films that formed by drying L-(+)-TA solution had a spherulite morphology with a needle-like structure (Fig. 1E).

Composite L-(+)-TA/CNC films with $4.0 \leq R \leq 6.0$ exhibited a Maltese cross and a radial concentric ring pattern, with ring color periodically alternating between orange and blue (Fig. 1, B to D). At $R < 3.5$, no periodic bands were observed, and at $R = 3.5$, the rings were limited to only a small region of the film. At $R > 6.0$, films with dendritic crystal structures were formed (fig. S1). When composite films were formed from a mixture of CNCs and D-(−)-tartaric acid, the formation of concentric bands was observed in <15% of the films, and it was completely suppressed in films containing racemic and enantiomeric mixtures of L-(+)- and D-(−)-tartaric acid (fig. S2). We also verified that concentric ring patterns did not form from CNC mixtures with other small chiral molecules such as D-(−)-glucose or D-(−)-mannitol or achiral citric acid (fig. S3). Later in the text, we focus on the films containing L-(+)-TA (referring to it as TA).

Imaging of drying TA/CNC suspensions under POM revealed that ring formation began from a nucleation point close to the film center from which periodic bands grew radially toward the edge of the film. The period, P, of the ring pattern was determined as the average distance between the middle lines of the consecutive rings with the same color, using POM images (fig. S4, A and B). The value of P depended on film composition and RH. Figure 2 (A to C) shows that with R increasing from 4.5 to 5.5 (that is, increasing TA concentration), the value of P changed from 126 ± 13 to 271 ± 40 μm, respectively, at the expense of the increasing width of the blue rings, while the width of the orange bands was invariant at 25 ± 1 μm.

With increasing RH, the value of P became larger (Fig. 2, D to F); however, the range of RH at which ring patterns formed was limited. At RH ≥ 44%, the films did not dry, due to the highly hygroscopic nature of TA (*36*), while at RH = 11%, rapid drying of the TA/CNC suspensions yielded films with a grainy, crystalline morphology (fig. S1).

To follow the growth dynamics of the formation of periodic rings, we recorded the evolution of the spatiotemporal pattern upon water evaporation for the liquid films (movie S1). Figure 2 (G to J) shows the snapshots of the liquid TA/CNC film taken at different drying times, while Fig. 2K shows the corresponding temporal variation in the distance, r, from the nucleation point to the outer edge of the dry film. As time progressed, the film dried radially to its edge with a constant velocity, which produced equidistant bands, as indicated by the nearly linear slope of the graph in Fig. 2K. To confirm that the bands were equidistant, we used Jablczynski's spacing law, which describes the formation of Liesegang rings from a central nucleation point (*37*). The spacing coefficient approached unity in films with varying R (fig. S4, C to F).

To characterize the composition of alternating rings in the composite films, we labeled CNCs with a covalently attached fluorescein isothiocyanate (FITC) dye, added 0.20 weight % (wt %) of FITC-labeled CNCs to the CNC suspension, and formed composite films from the mixture of this suspension with TA at $R = 5.0$. Figure 3 (A and B) shows a fluorescence microscopy image of the TA/CNC

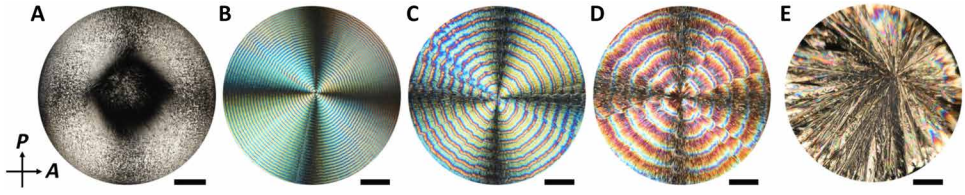

Fig. 1. POM images of CNC, TA/CNC, and TA films. POM images of films formed from (**A**) a CNC suspension; (**B** to **D**) TA/CNC suspensions with (left to right) R of 4.0, 5.0, and 6.0; and (**E**) a TA solution. Films were formed at 22°C and RH = 23%. The concentration of CNCs in (A) to (D) was 3 wt %, and the concentration of TA solution in (E) was 11.3 wt % (750 mM). All films were dried for 24 hours. Scale bars, 420 μm.

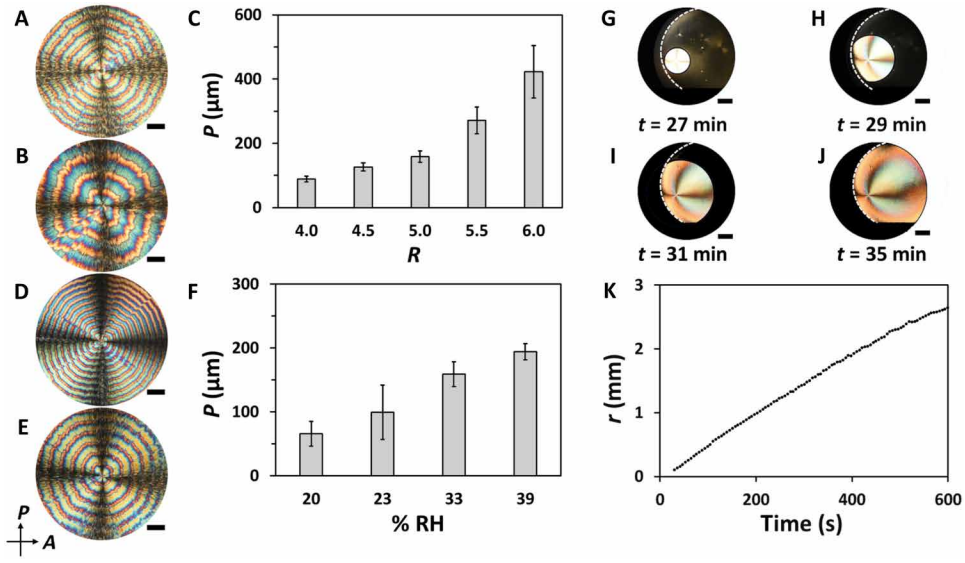

Fig. 2. Characterization of ring patterns in TA/CNC films. (**A** and **B**) POM images of films formed at *R* of 4.5 (A) and 5.5 (B). (**C**) Variation in the average period, *P*, of the ring pattern, plotted as a function of *R*. In (A) to (C), films were formed at RH = 33%. (**D** and **E**) POM images of films formed at RH = 23% (D) and 33% (E). (**F**) Variation in the average period, *P*, of the ring pattern, plotted as a function of RH. (D to F) Films were formed at *R* = 5.0. Error bars in (C) and (F) represent SDs for nine samples. Scale bars (A, B, D, and E), 300 μm. (**G** to **J**) POM images of a liquid TA/CNC film (*R* = 4.5, RH ≈ 21%), taken at various drying times. The white dashed lines show the outline of the drying droplet circumference. (**K**) Variation in the distance, *r*, from the nucleation point to the outer edge of the drying film, plotted as a function of time. Scale bars (G to J), 500 μm.

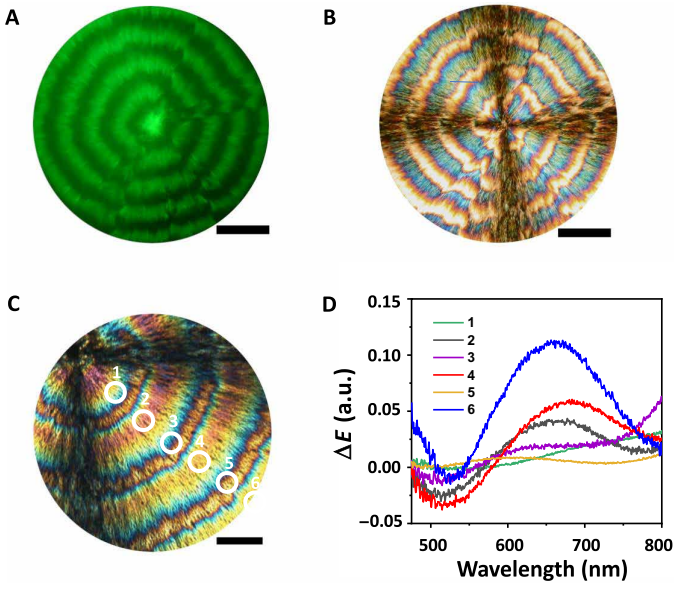

Fig. 3. Characterization of the composition of periodic bands in the composite film. (**A**) Fluorescence microscopy and (**B**) POM images of TA/FITC-CNC films formed at *R* = 5.0 and RH = 33%. Scale bars (A and B), 150 μm. (**C** and **D**) The variation in Δ*E* of the TA-rich bands (labeled as 1, 3, and 5) and CNC-rich bands (labeled as 2, 4, and 6) in (C). The Δ*E* spectra in (D) are collected from the regions marked in (C). Scale bar (C), 100 μm. a.u., arbitrary units.

film and a corresponding POM image, respectively. In Fig. 3A, alternating bright and dark green rings correspond to CNC-rich and CNC-deprived regions, respectively. On the basis of the analysis of fluorescence intensity of these bands and assuming a similar behavior of CNCs and FITC-CNCs, we estimated the relative concentration of CNCs in the CNC-enriched and CNC-depleted regions to be 67 ± 22 and 31 ± 11%, respectively (fig. S5). By comparing POM and fluorescence images of the composite films, we conclude that the narrow orange bands and wide blue bands in POM images were CNC enriched and CNC deprived (or TA enriched), respectively (Fig. 3, A and B).

The composite films were characterized by acquiring spectra of differential transmission Δ*E* of circularly polarized light of opposite handedness through ~50-μm-radius circular areas (see Materials and Methods). For spatially heterogeneous films, these spectra could have effective contributions from circular dichroism, differential scattering, and reflection of the two opposite-handedness circular polarizations, as well as the apparent change of polarization states. In Fig. 3C, the CNC-rich regions are marked as 2, 4, and 6, while the TA-rich regions are labeled as 1, 3, and 5. In Fig. 3D, the corresponding spectra acquired from the CNC-rich regions exhibited a strong Δ*E* signal, with intensity increasing for rings closer to the film circumference. The spectral position of the Δ*E* peak in the range of 660 to 680 nm correlated with that reported for Ch-CNC films (*32*, *33*, *38*). Films prepared from TA-free CNC suspension under similar RH conditions had weak Δ*E* signal (fig. S6A). In contrast, the value of Δ*E* for TA-rich regions in the spectral range of 600 to 725 nm was similar to that of the pristine TA films (fig. S6B).

Figure 4 (A and B) shows representative scanning electron microscopy (SEM) images of the film cross section of the CNC-rich and TA-rich regions, respectively. The stripe morphology of the CNC-enriched region in the cross section of the fractured film (roughly in the middle of the CNC-rich region) resembled the structure of pristine Ch-CNC films (*39*). The CNCs were largely oriented parallel to the plane of the film and perpendicular to the helical axis. Elongated TA-rich bundles with a diameter of 0.31 ± 0.03 μm were aligned in

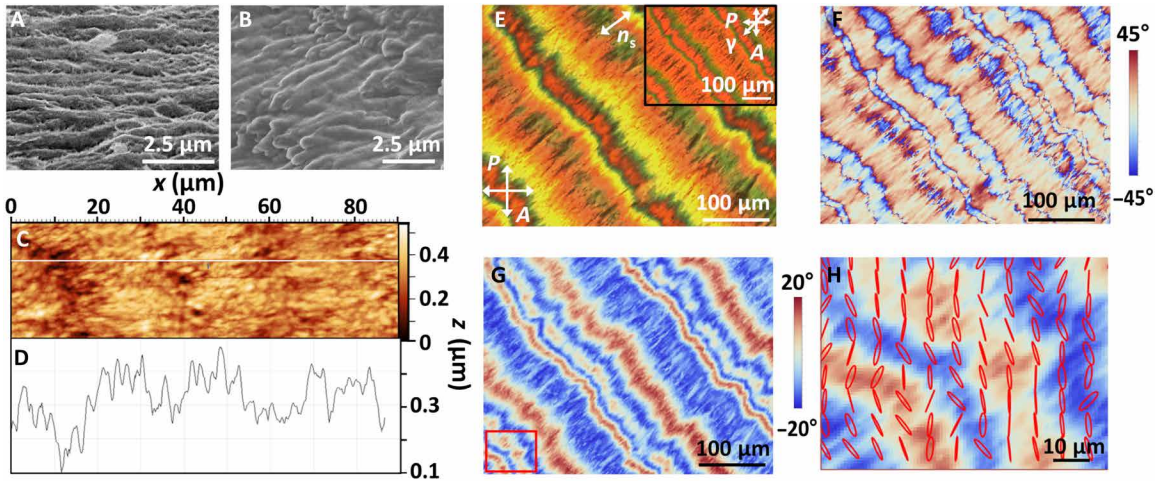

Fig. 4. Structure and topography of the composite films. (**A** and **B**) SEM images (taken at an oblique angle) of the cross section of the CNC-rich (A) and TA-rich (B) regions of the fractured film formed at $R = 4.5$ and RH = 23%. (**C**) AFM height image and (**D**) height profile of the TA/CNC film formed at $R = 4.5$ and dried at RH = 23%. (**E**) POM image of TA/CNC film prepared at $R = 5.0$ and RH = 33%, taken without and with [inset of (E)] a 530-nm phase retardation plate. The yellow and light orange colored regions are identified as TA-rich regions, while the red and green regions represent CNC-rich regions. The double-headed arrow in (E) indicates the average direction, n_s, of radially aligned TA-rich bundles in the film. (**F** to **H**) Polarimetry analysis of the TA/CNC film showing the distributions of orientation of the long axis of polarization ellipse χ (F) and ellipticity *e* (G) for the light transmitted through the film. The polarization states of the light transmitted from the region marked with red square in the bottom left of (G) are indicated by the red symbols overlaid on the image in (H). The ellipse and line symbols qualitatively represent elliptically and linearly polarized light, respectively.

the radial direction in the TA-enriched phase. The topography of the surface of the composite film was examined using atomic force microscopy (AFM). Figure 4 (C and D) shows the AFM image and height profile of the film surface, respectively, with the average ridge-to-well distance of 0.21 ± 0.07 μm. Furthermore, Fig. 4C and fig. S7 show elongated bundles that are packed radially in the TA-rich regions, consistent with their orientation in the film cross section (Fig. 4B).

Figure 4E shows a high-magnification POM image of the film, with the TA-rich regions (yellow and light orange color bands) and CNC-rich regions (red and green color bands). The TA bundle surface alignment direction, n_s, is represented by a double-headed arrow, indicating a 45° alignment with respect to the polarizer, *P*. The image shown in the inset of Fig. 4E was taken after inserting a 530-nm retardation plate into the POM setup, with the slow axis of the plate aligned at 45° to the polarizer, P. With the insertion of the retardation plate, the color of the TA-rich regions changed from yellow in Fig. 4E to red in the inset of Fig. 4E, indicating an increase in the retardation for the transmitted light, due to the alignment of TA-enriched bundles parallel to the slow axis of the plate. This color change, with the insertion of the retardation plate, revealed the radial bundle alignment consistent with the SEM and AFM analysis of the film.

We also performed polarimetry imaging to map out the variation in the polarization state of transmitted light (section S8), as illustrated in Fig. 4 (F to H). The film was illuminated with a 532-nm linearly polarized light with a polarization state set parallel to the vertical edge of the images. The variation in the orientation of the principal axis of polarization ellipse, χ, and the ellipticity angle, *e*, for the light transmitted through different film regions is represented by the color-coded images shown in Fig. 4 (F and G), respectively. The polarization states of the light transmitted through the region marked with a red square in Fig. 4G are indicated by the small overlaid ellipse and line symbols in Fig. 4H, representing the elliptically and linearly polarized states of the transmitted light, respectively. The orientations of these two symbols represent the orientation of the long axis of the polarization ellipse, χ, for the light transmitted in the respective regions in Fig. 4G. Analysis of the polarimetry image revealed modulation in the polarization state for the beam transmitted through the film, which resulted in the polarized interference of light under crossed polarizers, consistent with the colored fringes in the respective POM images in Fig. 4E. Both POM and polarimetry experiments revealed the orientational order in TA-rich ring-banded regions, synchronously with the modulation of the chemical composition in the film.

The intensity of light transmitted through crossed polarizers that sandwich a heterogeneous optically anisotropic medium of varying thickness scales as $I \propto \sin^2\left(\frac{\pi}{\lambda}\int_0^{h(r)} \Delta n(z,r)\,dz\right)$, where $\Delta n(z,r)$ and $h(r)$ are the effective birefringence dependent on the radial r and vertical z coordinates and film thickness that varies with r, respectively, and λ is the wavelength of light. Thus, the rings with constructive polarized interference appear bright and colored (Fig. 4E) due to the difference in polarized interference conditions for different wavelengths. Considering relatively small variations in film thickness (as shown in Fig. 4D), the variation in the optical retardation of the rings is attributed to the spatial modulation of the effective film birefringence $\Delta n(z,r)$ related to the CNC and TA concentrations and their structural organization within the stripes. Polarimetric analysis (Fig. 4, F to H) revealed the modulation in the polarization state for the beam transmitted through the film. This light-matter interaction within the POM patterns emerges from a combination of optical rotation and linear birefringence, spatially modulated due to the partial separation of CNCs and TA, accompanied by the orientational structural organization of both CNCs and elongated TA-enriched bundles. While phase separation takes place

mainly along the radial *r* direction, the structural features formed by CNCs and TA also vary along the film's depth which cannot be spatially reconstructed at the nanoscale solely by two-dimensional (2D) optical polarimetry characterization, providing an interesting example of complex out-of-equilibrium organization of interest for future studies.

Small-angle x-ray scattering (SAXS) was used to probe the structure of the TA/CNC films in the transmission mode (Fig. 5A). An x-ray beam with a size of 220 μm by 50 μm was used to scan the entire film area for SAXS mapping (section S9). We performed a quantitative analysis using the variation of the scattering intensity profile $I(\omega)$ with the azimuthal angle ω (defined within the vertical detector plane with respect to the horizontal direction; Fig. 5B). More specifically, we computed the 2D orientation distribution function (ODF), $f(\omega)$, which reflects the probability of the scatterers to be aligned in a particular direction (*40*, *41*) and is calculated as $f(\omega) = I(\omega) / \int_0^{\pi} I(\omega)\, d\omega$. Figure 5C shows the ODF for a typical examined spot of the TA/CNC film. We then fitted the ODF profiles (Fig. 5C) (*42*, *43*) at every examined spot of the SAXS scan and extracted the most probable angle ω_0 at each spot. This value of ω_0 determined the orientation of the anisotropic scatterers, $\theta_{scatter}$, for all spots of the scanned region. We note that for the elongated scatterers, the scattering angle ω_0 corresponds to the orientation ω_0 +90° in real space. Figure 5E shows $\theta_{scatter}$ mapping on the film (Fig. 5D). The anisotropic scatters followed a radial alignment, consistent with the AFM, SEM, and polarimetry imaging results in Fig. 4. Furthermore, to evaluate the orientation of anisotropic species in the film, the orientation order parameter, *S*, in the plane of the film was computed (*40*, *41*), with $S = 1$ for the perfect alignment and $S = 0$ for a randomly oriented system (Fig. 5E). Owing to the radial arrangement of anisotropic bundles, the extracted value of ω_0 was used as the reference direction to determine an order parameter at every spot of the SAXS scan, as shown in Fig. 5 (D and E). Figure 5E shows that the main area of the film exhibited $S \approx 0.2$. Notably, this order parameter was averaged over both the TA-rich and CNC-rich regions, since the x-ray beam dimensions are larger than the width of individual concentric rings. We ascribe anisotropy to the radial alignment of bundles in the TA-rich regions, since the results of optical characterization of the films in Fig. 4 (D and E) show that the CNC-rich regions had a Ch structure. SAXS mapping in Fig. 5E showed a gradual decrease of *S* with increasing distance from the nucleation center, consistent with a stronger contribution of the Ch-CNC regions shown in Fig. 3D.

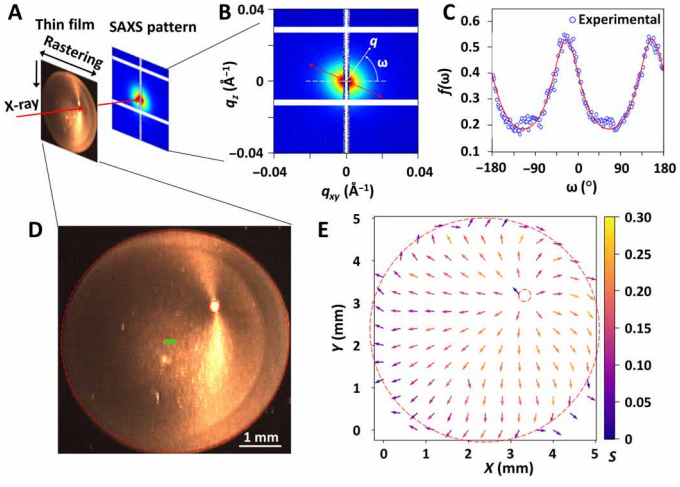

Fig. 5. Characterization of local anisotropy of the TA/CNC film by SAXS. (**A**) Schematic illustration of the SAXS rastering measurement for SAXS mapping of the film. (**B**) A typical SAXS pattern with a definition of the azimuthal angle ω. (**C**) 2D ODF $f(\omega)$, calculated from the SAXS pattern in (B), shows the anisotropic features along the most probable angle, denoted by ω_0, which provides information about the orientation within the film. The value of $f(\omega)$ is fitted using an ad hoc order parameter (red curve), described in section S9. (**D**) A photograph of the film taken during the SAXS measurement with dashed circles showing the circular edge of the dried droplet and the center of the concentric rings. The green rectangular box in the center of the film represents the size and shape of the x-ray beam. (**E**) Orientations of anisotropic scatterers, probed by the SAXS measurements and mapped on the entire area of the film. The direction of each arrow indicates the orientation in that location. The color represents the orientation order parameter in 2D, termed *S*, with the scale shown on the right. The dashed circles correspond to the circular edge of the film and the center of the concentric rings, similar to those shown in (D). The film was prepared at $R = 5.0$ and RH = 23%.

Numerical model

For the phase-separating TA/CNC suspension, we developed a kinetic model, which is generally applied to reaction-diffusion systems. The dynamics of the periodic pattern formation with two types of building blocks (CNCs and TA) was described as a set of differential equations that have a form

$$\frac{\partial c_i}{\partial t} = D_i \nabla^2 c_i + r_i(c_1, c_2, \ldots c_N) \quad (1)$$

where c_i, D_i, and r_i are the concentrations, the diffusion coefficients, and the rates of concentration change of the *i*th chemical compound, respectively; ∇ is the nabla operator; and *N* is the number of chemical species in the system. The left-hand side of Eq. 1 describes the concentration change of the chemical species in time. The first and the second terms in the right-hand side of Eq. 1 describe the concentration changes due to the diffusion and reaction of the species, respectively. The solution of Eq. 1 provides the spatiotemporal pattern formation in the TA/CNC film.

In our work, the drying TA/CNC suspension contained six species ($N = 6$), that is, the dissolved TA (A), the nuclei of precipitated TA (B), the crystals of TA in the TA-rich phase (C), the suspended individual CNCs (D), the TA-CNC clusters (E), and the CNC-enriched phase (F) (*44*). The process of periodic pattern formation had the following steps with the corresponding reaction rates v_1 to v_7 and rate constants k_1 to k_7

$$\mathrm{A} + \mathrm{B} \rightarrow 2\mathrm{B}, v_1 = k_1 ab, k_1 = 10^3 \quad (2)$$

$$\mathrm{B} + \mathrm{B} \rightarrow 2\mathrm{C}, v_2 = k_2 b^2, k_2 = 10^2 \quad (3)$$

$$\mathrm{B} + \mathrm{C} \rightarrow 2\mathrm{C}, v_3 = k_3 bc, k_3 = 10^2 \quad (4)$$

$$\mathrm{B} + \mathrm{D} \rightarrow \mathrm{E}, v_4 = k_4 bd\Theta(d - d^*), k_4 = 10^2 \quad (5)$$

$$\mathrm{B} + \mathrm{D} + \mathrm{E} \rightarrow 2\mathrm{E}, v_5 = k_5 bde\Theta(e - e^*), k_5 = 10^{-1} \quad (6)$$

$$\mathrm{E} + \mathrm{E} \rightarrow 2\mathrm{F}, v_6 = k_6 e^2, k_6 = 1 \quad (7)$$

$$E + F \rightarrow 2F, v_7 = k_7 ef, k_7 = 10^3 \quad (8)$$

where a, b, c, d, e, and f are the concentrations of the chemical species of A, B, C, D, E, and F, respectively; Θ is the Heaviside step function; and d^* and e^* are the threshold concentrations for the formation of TA-CNC clusters, respectively (Eqs. 5 and 6). The value of r_i in Eq. 1 is calculated using stoichiometric coefficients and reaction rates as $r_i = \sum_{j=1}^{7} \left(\upsilon_j^r - \upsilon_j^l\right) v_j$, where υ_j^r and υ_j^l are the stoichiometric coefficients of the ith compound at the right- and left-hand sides in the jth equation, respectively, and v_j is the reaction rate of the jth process. Equations 2 and 4 describe the autocatalytic formation of TA nuclei and TA crystals, respectively. Equation 3 describes the process of the formation of TA crystals from the TA nuclei. The model comprises two concentration threshold-limited steps (Eqs. 5 and 6), which describe the formation of TA-CNC clusters. These clusters result in the CNC-enriched phase (Eqs. 7 and 8). Figure S10 shows the schematic representation of the mechanism.

We solved the set of partial differential equations (Eq. 1) numerically by using the method of lines technique on an equidistant grid in a polar coordinate system (*45*). The finite difference spatial discretization method was combined with a forward Euler method for the integration in time of the set of ordinary differential equations. We applied the following initial conditions $a(t = 0, r) = 1.0$, $b(t = 0, r) = 0$, $c(t = 0, r) = 0$, $d(t = 0, r) = 1.0$, $e(t = 0, r) = 0$, and $f(t = 0, r) = 0$ to reflect the initial experimental conditions, when TA (A) and CNCs (D) were uniformly distributed in the mixed suspension. To initiate pattern formation, we increased the concentration of B at $r = 0$ at $t = 0$, i.e., $b(t = 0, r = 0) = 1.0$. We used no-flux and Dirichlet boundary conditions for all chemical species at $r = 0$ and $r = L$, respectively, where L is the length of the simulation domain.

Figure 6 shows that the numerical model qualitatively reproduced the experimental findings: The threshold-limited phase separation of TA and CNCs (Eqs. 5 and 6) produced periodic TA-rich and CNC-rich ring-type regions (Fig. 6, A and B, respectively). The model predicted a finite constant velocity of the moving front of the edge of the pattern (Fig. 2K) due to reactions described by Eqs. 2 to 8 (see movie S1).

DISCUSSION

Generally, in multicomponent precipitation/diffusion-governed systems, the sizes of the components are in the same range, e.g., they are represented by either molecules (*12*, *13*) or NPs (*23*). Our work provides the first evidence for the periodic ring-banded structures formed by two components with dimensions differing by several orders of magnitude. We stress the difference between the results observed in our work and several other phenomena that yield ring patterns, or even dual-scale patterns, in drying liquid films. Periodic "coffee ring" patterns originate from particle deposition at the contact line (the outer edge of a drying suspension) due to their periodic pinning to the substrate (*46*, *47*), while in our work, the concentric ring pattern evolved close to the center of the film. The nucleation of the ring pattern in the film center, as well as a low temperature difference across the liquid layer (caused by water evaporation), did not favor the Rayleigh-Bénard convection (*48*). Notably, our results are also in marked difference with pattern formation in Belousov-Zhabotinsky autocatalytic oscillatory chemical reactions (*49*), since concentric ring patterns formed via phase separation, diffusion, and precipitation of CNC-rich and TA-rich phases rather than a chemical reaction.

In our work, the evaporation of water from the TA/CNC suspension resulted in saturation of CNCs and TA in the mixture, accompanied by their local phase separation and subsequent precipitation of the phase enriched with a particular component. The threshold-limited steps (described by Eqs. 5 and 6) led to the saturation of CNC and phase separation close to the film center, thus creating a nucleation zone (a bright green spot in Fig. 3A and movie S1). These steps, as well as CNC diffusion from the mixed suspension toward the CNC-rich phase, depleted the neighborhood of the nucleation point from the CNCs, thereby stopping the growth of the CNC-rich ring-type band. Next, the threshold concentration of TA was reached in the region adjacent to the CNC-rich region, followed by the TA diffusion to this zone, and the TA-rich phase precipitated as a ring-type band. Then, the CNC saturation was achieved, again, in the region adjoining the TA-enriched phase and a new CNC-rich band. This repetitive phase separation/precipitation/diffusion-governed process resulted in rhythmic alternation of CNC-rich and TA-rich concentric ring-type bands. The developed kinetic model reproduced qualitatively the experimental results, that is, constant periodicity and growth of the rings in the radial direction, which is the manifestation of the finite constant velocity of the pattern formation front.

The morphology of the composite films was controlled by varying the composition of the TA/CNC suspension and RH. At large R values (corresponding to the high TA content in the mixture), TA crystallization suppressed the formation of CNC-enriched ring-banded regions. At small R values (that is, at low TA concentration in the mixture), the amount of TA was insufficient for phase separation and thus the formation of alternating ring-type regions. The value of RH controlled the rate of water evaporation from the liquid film, thus affecting the time within which the system reached the

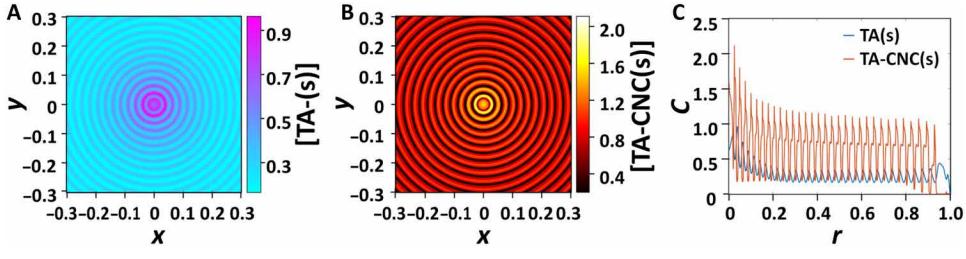

Fig. 6. Numerical simulations of ring pattern formation. (**A**) Spatial distribution of TA-(s), (**B**) spatial distribution of CNCs, and (**C**) concentration profiles of TA and CNCs in alternating ring-type bands. In the simulations, the following parameters were used: $D_A = 10^{-1}$, $D_B = 10^{-2}$, $D_D = 10^{-2}$, $D_E = 10^{-4}$, $d^* = 0.8$, and $e^* = 0.2$. The grid spacing (Δr) and time step (Δt) in the numerical simulations were 10^{-3} and 1.8×10^{-8}. All parameters and variables are in dimensionless units.

saturation state, as well as the extent of CNC and TA diffusion, with wider bands formed at higher RH. We note that the addition of TA to the CNC suspension resulted in the reduction in ζ-potential of CNCs and could lead to the increase in suspension viscosity (*50*). Similarly, the evaporation of water from the mixed TA/CNC suspension caused an increase in viscosity. Our simulations showed that the periodic ring patterns did not qualitatively change with increasing viscosity and hence reducing diffusion coefficients of the compounds.

The CNC-enriched and TA-enriched ring-banded regions had distinct structures. The CNC-enriched regions exhibited a Ch structure with characteristic optical properties. We speculate that slow evaporation of water (controlled by RH) and local (site-specific) increase in CNC concentration in the liquid film, due to phase separation, favored CNC assembly in the Ch structure. The TA-rich regions contained elongated TA-enriched bundles that are substantially thicker than the needle-like crystallite structures formed by pristine TA (Fig. 1E), which suggested the possibility of CNC embedding in these bundles, due to hydrogen bonding between TA and CNCs. The alignment of the bundles in the radial direction (confirmed in AFM, SEM, SAXS, and polarimetry experiments) was a result of shear induced by the evaporation of water from the liquid film.

MATERIALS AND METHODS

An aqueous 10.3 wt % CNC suspension was supplied by the University of Maine Process Development Center. Deionized water obtained from a Millipore Milli-Q water purification system was used to dilute the CNC suspension to a concentration of 6.9 wt %, which was equilibrated for 10 days to separate into upper isotropic and lower Ch phases. The Ch phase was removed with a glass pipet and used for experiments. L-(+)-TA (purity of >99.5%), D-(−)-tartaric acid (purity of >99%), lithium chloride, magnesium chloride hexahydrate, and potassium acetate salts and FITC isomer I were purchased from Sigma-Aldrich Canada. Potassium carbonate (anhydrous), calcium bromide hydrate, and sodium iodide dihydrate were purchased from Fisher Chemical. All chemicals were used without further purification.

Preparation of the composite films

Solutions of either L- or D-tartaric acid in deionized water with concentrations in the range of 5 to 1800 mM (0.075 to 27 wt %) were mixed with the CNC suspension to the final CNC concentration of 3 wt %. The ratio of mass concentrations, *R*, of TA to CNCs or D-(+)-tartaric acid to CNCs in the suspension or film varied from 3.0 to 9.0.

Borosilicate glass microscope coverslips (VWR International LLC) were washed subsequently with isopropanol, water, and ethanol and dried with filtered compressed air before use. Droplets of either L- or D-tartaric acid/CNC suspensions with a volume of 10 μl were deposited onto the glass slide using a 20-μl Eppendorf pipette at 21°C and RH ≈ 40% and immediately placed in a sealed chamber under controlled RH of 11, 18, 23, 33, 39, or 44% for 24 hours. The value of RH was controlled by introducing a saturated solution of a particular salt in the chamber and equilibrating it for 24 to 48 hours (*51*). The salts and their respective values of RH were LiCl (11%), $CaBr_2{\cdot}xH_2O$ (18%), CH_3CO_2K (23%), $MgCl_2$ (33%), NaI (39%), and K_2CO_3 (44%).

Covalent attachment of FITC to CNCs was conducted, as described elsewhere (*52*). An aqueous 3.11 wt % CNC suspension was mixed with 25 ml of 1.0 M NaOH solution and epichlorohydrin (7.05 ml, 0.28 mol/g of CNC) and heated at 60°C for 1 hour. The excess epichlorohydrin was removed from the epoxy-CNC mixture by 3 cycles of centrifugation (6000*g*, 10 min) and resuspension in deionized water (15 ml). The pH of the epoxy-CNC suspension was readjusted to 12.0 (pH meter, Mettler Toledo) with 50% (w/v) NaOH. Excess ammonia hydroxide (12 ml, 28 wt %, 5 ml/g of CNC) was added, and the mixture was heated at 60°C and stirred for 3 hours. Subsequently, ammonium hydroxide was removed by 3 cycles of centrifugation (6000*g*, 10 min), and NH_2-CNCs were redispersed in 15 ml of deionized water.

FITC (37 mg, 0.32 mmol/g of CNC) was dissolved in 2 ml of dimethyl formamide and added to a 15-ml NH_2-CNC suspension mixed with 15 ml of $NaHCO_3$ buffer (100 mM, pH 9.0). The mixture was stirred overnight in the dark and dialyzed for 5 days against deionized water (changed twice daily) using a cellulose dialysis tubing membrane (14,000 molecular weight cutoff; Sigma-Aldrich) until FITC was no longer identified in deionized water using ultraviolet-visible spectroscopy. The suspension was sonicated for 20 min in an ice bath and filtered with a 0.45-μm syringe filter. The pH of the FITC-CNC was adjusted to 11.0 using $NaHCO_3$ buffer (100 mM), and the amount of FITC attached to CNCs was determined using a calibration curve generated using standard FITC solutions in ammonium hydroxide (28 wt %, pH 11.0). The molar extinction coefficient, ε_{490}, for FITC amide was calculated to be $7.1 \times 10^4\ M^{-1}\ cm^{-1}$. The concentration of FITC was 0.10 molecules of FITC per square nanometer of CNC.

Composite films were prepared by mixing an aqueous TA solution and a mixed suspension of CNCs (5.01 wt %) and FITC-CNCs (0.20 wt %) (mixed to form a 3.00 wt % suspension). In the dry film, the concentration of FITC-CNC was 0.61%.

Characterization of CNCs

Transmission electron microscopy (TEM) experiments were conducted to determine the average CNC length and diameter, using a Hitachi HT7700 at 60 kV. Droplets of aqueous CNC suspension (0.001 wt %) were deposited onto a lacey carbon film 300-mesh copper grid and left until dried.

The electrokinetic potential (ζ-potential) of CNCs was measured using a Malvern Zetasizer Nano ZS instrument at 22°C. For each sample, nine measurements have been performed. The degree of sulfation of CNCs (sulfur half-ester content reported as millimole sulfate per kilogram of CNC) was determined by conductometric titration, as described elsewhere (*53*). Briefly, sulfate half-ester groups of CNCs in a 2 wt % suspension were protonated using a Dowex Marathon C hydrogen form ion exchange column (Supelco). Subsequently, the protonated CNCs were titrated against a standardized 0.1 M NaOH solution using an EcoMet 65 conductivity meter.

Characterization of composite film structure

POM imaging was carried out in transmission mode, using an optical microscope (Olympus BX51), with images acquired using a Nikon D7200 camera. The dimensions and structure of the composite droplets were analyzed using the software ImageJ. The fluorescence images of the composite films containing FITC-labeled CNCs were acquired using an optical microscope (Olympus BX51) with an FITC

filter cube (U-N41001 HQ:F), with an excitation wavelength of 480 ± 23 nm.

The preparation of samples for SEM imaging of the composite films was performed by depositing a droplet of TA/CNC (R = 4.5) suspension on a silicon wafer and drying at RH = 23%. Before deposition, the wafer was washed with water and ethanol and dried with filtered compressed air. The samples were imaged using the FEI Quanta FEG 250 environmental scanning electron microscope under high vacuum at 3 kV. To obtain fractured films, silicon wafers with deposited films were cut with a diamond-tipped glass cutter. The fractured films affixed to the silicon wafers were mounted on 90° specimen mounts using a conductive carbon tape.

AFM experiments were carried out on films formed by depositing a droplet of TA/CNC (R = 4.5) on a silicon wafer and drying at RH = 23%. The samples were imaged using a Dimension atomic force microscope (Bruker Corporation). Measurements were performed under ambient environment in tapping mode using aluminum-coated silicon tips with a radius of 8 nm, resonance frequency of ~325 kHz, and force constant ≈ 40 N/m (HQ:NSC15/Al BS, MikroMasch). Image analysis was performed using Gwyddion and ImageJ software. All images were flattened, corrected, and stitched using the built-in Gwyddion functions.

Spatially resolved measurements of ΔE for the films were performed on an inverted optical microscope (Olympus IX71). The samples were illuminated with a 50-μm-radius beam of collimated light from a white light source using a pinhole arrangement. The polarization state of the illumination light was controlled using a broadband polarizer and an achromatic quarter waveplate, placed immediately before the sample. The transmitted light through the sample was collected using a 20× objective (Olympus SLMPlan) and guided to a spectrometer (Ocean Optics, USB 2000-FLG) using an optical fiber. The differences between the light extinction by the films for the left (ε_l) and right (ε_r) circularly polarized components of the illumination light were measured separately, giving $\Delta E = \varepsilon_l - \varepsilon_r$ (*54*, *55*).

The polarimetric imaging of the TA/CNC samples was performed on an upright microscope (Olympus BX51) using a 40× (Olympus UPlan FLN) objective to image. The film was illuminated with a linearly polarized light (aligned vertically to the sample plane) at 532 nm, and the polarization state of the light transmitted through the film was analyzed using a quarter waveplate (AQWP05M-600, Thorlabs) inserted below the analyzer A (aligned parallel to the incident polarization of Fig. 4E). To map out the variations in the polarization state of the transmitted light, the images of the film were collected by rotating the fast axis of the waveplate from 0° to 180° in steps of 22.5°. The ellipticity, e, and orientation of the polarization ellipse, χ, for the transmitted light through the sample were estimated using these images by numerical methods (Supplementary materials).

SAXS experiments were performed at the Soft Matter Interfaces (SMI, 12-ID) beamline at the National Synchrotron Light Source II at Brookhaven National Laboratory. The films were cast on a coverslip (using earlier described methods) and probed by an x-ray beam with a photon energy of E = 18.25 keV (x-ray wavelength λ = 0.67940 Å) in the transmission mode, where the beam was along the surface-normal direction of the coverslip. The beam size was 220 μm by 50 μm, and the films were scanned in a snake-like scan path with a step size of 400 μm in horizontal and vertical directions. The scattering pattern at each scanning spot was collected using a 2D detector (Pilatus 1M; 172 μm by 172 μm per pixel) placed downstream with a sample-to-detector distance of 8.3 m. The exposure time for each scan spot was 0.5 or 1.0 s since radiation damage was observed for longer exposure time. Scattering from the blank coverslip was collected as a background and subtracted from the scattering pattern before further data analysis.

SUPPLEMENTARY MATERIALS

Supplementary material for this article is available at http://advances.sciencemag.org/cgi/content/full/7/16/eabe3801/DC1

REFERENCES AND NOTES

1. I. R. Epstein, B. Xu, Reaction–diffusion processes at the nano- and microscales. *Nat. Nanotechnol.* **11**, 312–319 (2016).
2. T. Saha, M. Galic, Self-organization across scales: From molecules to organisms. *Philos. Trans. R. Soc. Lond. B Biol. Sci.* **373**, 20170113 (2018).
3. P. Ortoleva, E. Merino, C. Moore, J. Chadam, Geochemical self-organization I; reaction-transport feedbacks and modeling approach. *Am. J. Sci.* **287**, 979–1007 (1987).
4. E. Nakouzi, O. Steinbock, Self-organization in precipitation reactions far from the equilibrium. *Sci. Adv.* **2**, e160114 (2016).
5. S. A. Sozinov, A. N. Popova, L. V. Sotnikova, Self-organization of hexane-insoluble asphaltenes of coal pitch. *Coke Chem.* **62**, 411–415 (2019).
6. K. Iwamoto, S. I. Mitomo, M. Seno, Rhythmic crystallization of ascorbic acid precipitated from its methanol solutions. *J. Colloid Interface Sci.* **102**, 477–482 (1984).
7. J. A. Armas, K. J. Reynolds, Z. M. Marsh, M. Stefik, G. E. Scott, S. Zhang, Ring-banded spherulitic crystals of poly(3-butylthiophene) via controlled solvent evaporation. *Macromol. Chem. Phys.* **219**, 1800204 (2018).
8. L. C. Anderson, H. Brumberg, R. H. Marchess, Morphology of poly-L-alanine spherulites. *Nature* **216**, 52–54 (1967).
9. P. J. Feeney, R. G. Gilbert, D. H. Napper, Periodic nucleation processes in emulsion polymerization systems. *J. Colloid Interface Sci.* **107**, 159–173 (1985).
10. P. L. Perrotta, F. W. Ginsburg, C. I. Siderides, V. Parkash, Liesegang rings and endometriosis. *Int. J. Gynecol. Pathol.* **17**, 358–362 (1998).
11. M. Rosenthal, G. Portale, M. Burghammer, G. Bar, E. T. Samulski, D. A. Ivanov, Exploring the origin of crystalline lamella twist in semi-rigid chain polymers: The model of Keith and Padden revisited. *Macromolecules* **45**, 7454–7460 (2012).
12. R. E. Liesegang, Über einige Eigenschaften von Gallerten. *Naturwiss. Wschr* **11**, 353–362 (1896).
13. R. E. Liesegang, Geschichtete Strukturen. *Z. Anorg. Allg. Chem.* **48**, 364–366 (1905).
14. H. Nabika, M. Itatani, I. Lagzi, Pattern formation in precipitation reactions: The Liesegang phenomenon. *Langmuir* **36**, 481–497 (2020).
15. T. Kovács, R. Szűcs, G. Holló, Z. Zuba, J. Molnár, H. K. Christenson, I. Lagzi, Self-assembly of chiral menthol molecules from a liquid film into ring-banded spherulites. *Cryst. Growth Des.* **19**, 4063–4069 (2019).
16. A. G. Shtukenberg, Y. O. Punin, E. Gunn, B. Kahr, Spherulites. *Chem. Rev.* **112**, 1805–1838 (2012).
17. B. A. Grzybowski, C. J. Campbell, Fabrication using 'programmed' reactions. *Mater. Today* **10**, 38–46 (2007).
18. M. Morsali, M. T. Ali Khan, R. Ashirov, G. Holló, H. T. Baytekin, I. Lagzi, B. Baytekin, Mechanical control of periodic precipitation in stretchable gels to retrieve information on elastic deformation and for the complex patterning of matter. *Adv. Mater.* **32**, 1905779 (2020).
19. C. J. Campbell, E. Baker, M. Fialkowski, A. Bitner, S. K. Smoukov, B. A. Grzybowski, Self-organization of planar microlenses by periodic precipitation. *J. Appl. Phys.* **97**, 126102 (2005).
20. S. K. Smoukov, A. Bitner, C. J. Campbell, K. Kandere-Grzybowska, B. A. Grzybowski, Nano- and microscopic surface wrinkles of linearly increasing heights prepared by periodic precipitation. *J. Am. Chem. Soc.* **127**, 17803–17807 (2005).
21. H. Ni, M. Pan, K. Shi, J. Zhou, M. Wu, Preparation of isometric Liesegang patterns and application in multi-pulsed drug release system. *J. Sol. Gel Sci. Technol.* **91**, 216–224 (2019).
22. G. M. Whitesides, B. Grzybowski, Self-assembly at all scales. *Science* **295**, 2418–2421 (2002).
23. I. Lagzi, B. Kowalczyk, B. A. Grzybowski, Liesegang rings engineered from charged nanoparticles. *J. Am. Chem. Soc.* **132**, 58–60 (2010).
24. H. Nabika, M. Sato, K. Unour, Liesegang patterns engineered by a chemical reaction assisted by complex formation. *Langmuir* **30**, 5047–5051 (2014).
25. R. Sultan, P. Ortoleva, F. DePasquale, P. Tartaglia, Bifurcation of the Ostwald-Liesegang supersaturation-nucleation-depletion cycle. *Earth Sci. Rev.* **29**, 163–173 (1990).

26. Y. Habibi, L. A. Lucia, O. J. Rojas, Cellulose nanocrystals: Chemistry, self-assembly, and applications. *Chem. Rev.* **110**, 3479–3500 (2010).
27. C. Schütz, J. R. Bruckner, C. Honorato-Rios, Z. Tosheva, M. Anyfantakis, J. P. F. Lagerwall, From equilibrium liquid crystal formation and kinetic arrest to photonic bandgap films using suspensions of cellulose nanocrystals. *Crystals* **10**, 199 (2020).
28. J. A. Kelly, M. Yu, W. Y. Hamad, M. J. MacLachlan, Large, Crack-free freestanding films with chiral nematic structures. *Adv. Opt. Mater.* **1**, 295–299 (2013).
29. G. Guidetti, S. Atifi, S. Vignolini, W. Y. Hamad, Flexible photonic cellulose nanocrystal films. *Adv. Mater.* **28**, 10042–10047 (2016).
30. B. Wang, A. Walther, Self-assembled, iridescent, crustacean-mimetic nanocomposites with tailored periodicity and layered cuticular structure. *ACS Nano* **9**, 10637–10646 (2015).
31. M. Gu, C. Jiang, D. Liu, N. Prempeh, I. I. Smalyukh, Cellulose nanocrystal/poly(ethylene glycol) composite as an iridescent coating on polymer substrates: Structure-color and interface adhesion. *ACS Appl. Mater. Interfaces* **8**, 32565–32573 (2016).
32. H. Thérien-Aubin, A. Lukach, N. Pitch, E. Kumacheva, Structure and properties of composite films formed by cellulose nanocrystals and charged latex nanoparticles. *Nanoscale* **7**, 6612–6618 (2015).
33. H. Thérien-Aubin, A. Lukach, N. Pitch, E. Kumacheva, Coassembly of nanorods and nanospheres in suspensions and in stratified films. *Angew. Chem. Int. Ed. Engl.* **54**, 5618–5622 (2015).
34. Y. Li, J. J. Suen, E. Prince, E. M. Larin, A. Klinkova, H. Thérien-Aubin, S. Zhu, B. Yang, A. S. Helmy, O. D. Lavrentovich, E. Kumacheva, Colloidal cholesteric liquid crystal in spherical confinement. *Nat. Commun.* **7**, 12520 (2016).
35. R. M. Parker, G. Guidetti, C. A. Williams, T. Zhao, A. Narkevicius, S. Vignolini, B. Frka-Petesic, The self-assembly of cellulose nanocrystals: Hierarchical design of visual appearance. *Adv. Mater.* **30**, 1704477 (2018).
36. C. Peng, M. N. Chan, C. K. Chan, The hygroscopic properties of dicarboxylic and multifunctional acids: Measurements and UNIFAC predictions. *Environ. Sci. Technol.* **35**, 4495–4501 (2001).
37. C. K. Jablczynski, Memoires presentes à la sociétié chimique. Les anneaus de Liesegang. *Bull. Soc. Chim. Fr.* **33**, 1592 (1923).
38. J. P. F. Lagerwall, C. Schütz, M. Salajkova, J. Noh, J. H. Park, G. Scalia, L. Bergström, Cellulose nanocrystal-based materials: From liquid crystal self-assembly and glass formation to multifunctional thin films. *NPG Asia Mater.* **6**, e180 (2014).
39. J. Majoinen, E. Kontturi, O. Ikkala, D. G. Gray, SEM imaging of chiral nematic films cast from cellulose nanocrystal suspensions. *Cellul.* **19**, 1599–1605 (2012).
40. J. P. Straley, Liquid crystals in two dimensions. *Phys. Rev. A* **4**, 675–681 (1971).
41. T. Rosén, R. Wang, C. Zhan, H. He, S. Chodankar, B. S. Hsiao, Cellulose nanofibrils and nanocrystals in confined flow: Single-particle dynamics to collective alignment revealed through scanning small-angle x-ray scattering and numerical simulations. *Phys. Rev. E* **101**, 032610 (2020).
42. W. Ruland, H. Tompa, The effect of preferred orientation on the intensity distribution of (*hk*) interferences. *Acta. Cryst. A* **24**, 93–99 (1968).
43. K. J. De France, K. G. Yager, T. Hoare, E. D. Cranston, Cooperative ordering and kinetics of cellulose nanocrystal alignment in a magnetic field. *Langmuir* **32**, 7564–7571 (2016).
44. H. K. Henisch, *Crystals in Gels and Liesegang Rings* (Cambridge Univ. Press, 1988).
45. W. E. Schiesser, *The Numerical Method of Lines* (Academic Press, 1991).
46. A. Gençer, C. Schütz, W. Thielemans, Influence of the particle concentration and Marangoni flow on the formation of cellulose nanocrystal films. *Langmuir* **33**, 228–234 (2017).
47. S. Srivastava, Z. A. Wahith, O. Gang, C. E. Colosqui, S. R. Bhatia, Dual-scale nanostructures via evaporative assembly. *Adv. Mater. Interfaces* **7**, 1901954 (2020).
48. E. Bodenschatz, W. Pesch, G. Ahlers, Recent developments in Rayleigh-Bénard convection. *Annu. Rev. Fluid Mech.* **32**, 709–778 (2000).
49. R. J. Field, E. Koros, R. M. Noyes, Oscillations in chemical systems. II. Thorough analysis of temporal oscillation in the bromate-cerium-malonic acid system. *J. Am. Chem. Soc.* **94**, 8649–8664 (1972).
50. T. Abitbol, D. Kam, Y. Levi-Kalisman, D. G. Gray, O. Shoseyov, Surface charge influence on the phase separation and viscosity of cellulose nanocrystals. *Langmuir* **34**, 3925–3933 (2018).
51. L. Greenspan, Humidity fixed points of binary saturated aqueous solutions. *J. Res. Natl. Bur. Stand.* **81**, 89–96 (1977).
52. M. Guo, S. Her, R. Keunen, S. Zhang, C. Allen, M. A. Winnik, Functionalization of cellulose nanocrystals with PEG-metal-chelating block copolymers via controlled conjugation in aqueous media. *ACS Omega* **1**, 93–107 (2016).
53. M. S. Reid, M. Villalobos, E. D. Cranston, Benchmarking cellulose nanocrystals: From the laboratory to industrial production. *Langmuir* **33**, 1583–1598 (2017).
54. A. Rodger, B. Nordén, *Circular Dichroism and Linear Dichroism* (Oxford Univ. Press, 1997).
55. L. D. Barron, *Molecular Light Scattering* (Cambridge Univ. Press, 2004).
56. P. Yeh, G. Gu, *Optics of Liquid Crystal Displays* (John Wiley & Sons, 1999).
57. R. J. Roe, *Methods of X-ray and Neutron Scattering in Polymer Science* (Oxford Univ. Press, 2000).

Acknowledgments: We thank I. Gourevich for assistance in SEM imaging experiments and W. Shi and G. Walker for assistance in AFM imaging experiments. This research used the SMI beamline (12-ID) of the National Synchrotron Light Source II and the Center for Functional Nanomaterials, which are U.S. DOE Office of Science Facilities at Brookhaven National Laboratory under contract no. DE-SC0012704. We acknowledge M. Zhernenkov and G. Freychet from the SMI beamline for the technical support with SAXS measurements **Funding:** E.K. thanks NSERC Canada (Discovery and Canada Research Chair Programs) for financial support of this work. I.L. acknowledges support by the National Research, Development, and Innovation Office of Hungary (NN125752 and K131425) and the BME Nanotechnology and Materials Science TKP2020 IE grant of NKFIH Hungary (BME IE-NAT TKP2020). I.I.S. and H.M. acknowledge the support of the U.S. NSF grant DMR-1810513. O.G. acknowledges support from the U.S. Department of Defense, Army Research Office, grant GG014598. **Author contributions:** E.K. and A.J.A. conceived the concept of this work and designed the experiments. A.J.A. formed the films required for all subsequent experiments; conducted POM, AFM, SEM, TEM, and fluorescence imaging experiments; analyzed data relevant in determining trends; and contributed to the interpretation of results. H.M. conducted polarimetry, ellipsometry, and spectroscopy experiments and contributed to the interpretation of results. H.Z. conducted SAXS experiments and contributed to the interpretation of results. I.L. designed the numerical model and contributed to the interpretation of results. G.H. measured the growth dynamics. I.I.S. contributed to the interpretation of POM, ellipsometry, and spectroscopy results. O.G. contributed to the interpretation of SAXS results. E.K., A.J.A., and I.L. wrote the manuscript with input from all authors. **Competing interests:** The authors declare that they have no competing interests. **Data and materials availability:** All data needed to evaluate the conclusions in the paper are present in the paper and/or the Supplementary Materials. Additional data related to this paper may be requested from the authors.

Submitted 22 August 2020
Accepted 2 March 2021
Published 16 April 2021
10.1126/sciadv.abe3801

Citation: A. J. Ackroyd, G. Holló, H. Mundoor, H. Zhang, O. Gang, I. I. Smalyukh, I. Lagzi, E. Kumacheva, Self-organization of nanoparticles and molecules in periodic Liesegang-type structures. *Sci. Adv.* **7**, eabe3801 (2021).

Science Advances

Self-organization of nanoparticles and molecules in periodic Liesegang-type structures

Amanda J. Ackroyd, Gábor Holló, Haridas Mundoor, Honghu Zhang, Oleg Gang, Ivan I. Smalyukh, István Lagzi and Eugenia Kumacheva

Sci Adv **7** (16), eabe3801.
DOI: 10.1126/sciadv.abe3801

Science Advances (ISSN 2375-2548) is published by the American Association for the Advancement of Science, 1200 New York Avenue NW, Washington, DC 20005. The title *Science Advances* is a registered trademark of AAAS.